Check for updates

All publication charges for this article have been paid for by the Royal Society of Chemistry

Divergent catalytic behaviors of assembled organogold(I) clusters derived from enyne cyclization†

Qian Liu, Xiao-Yi Zhai, Rui-Jun Jian and Liang Zhao [iD] *

Homogeneous gold catalysis has attracted much recent attention due to diverse activation modes of gold(I) towards unsaturated organic groups. Because of attractive aurophilic interaction, structural transformations of metalated species into high nuclear clusters are often proposed in gold catalysis, while to date little is known about their assembly behaviors and catalytic activity. In this work, based on stoichiometric Au(I)-mediated enyne cyclization reactions, we achieve a discrete vicinal dicarbanion-centered Au_4 intermediate and three assembled Au_{11}, Au_{28}, and Au_{14} clusters held together by several aryl dicarbanions. Spectral monitoring, kinetic and theoretical investigations confirm that these discrete and assembled intermediates display four different pathways upon catalyzing the cyclization reaction of the same 1,5-enyne substrate. The discrete Au_4 cluster undergoes a full protodeauration process to generate active $[Au(PPh_3)]^+$ species for catalytic use. In contrast, the net-like Au_{11} cluster experiences a substrate-induced dissociation to generate a semi-stable Au_{10} unit and an active $[alkyne-Au(PPh_3)]^+$ fragment for further transformation. The dumbbell-like Au_{28} cluster is prone to cleavage of the central Au−Au linkage and each Au_{14} moiety exposes a coordination unsaturated site to activate a substrate molecule. However, the synthetic closed-Au_{14} cluster with full ligand protection is no longer catalytically active.

Introduction

Structural evolution of catalytically active species widely exists in transition metal-catalyzed reactions.[1–3] Therein, mononuclear coordination metal catalysts experience the dissociation of labile ligands to recombine as polynuclear active species or undergo reduction by substrates, ligands, solvents, or additives to *in situ* generate metal clusters or even nanoclusters.[4–10] Not only can they directly activate substrates by exposing coordination unsaturated metal sites,[11,12] but they can also act as a reservoir to dissociate into smaller clusters as real active species for catalytic use.[13–15] Such metal clusters and nanoclusters show high diversity in nuclearity numbers, charges, configurations and peripheral ligands, promisingly allowing screening of highly active species to achieve excellent efficiency and selectivity.[16,17] Therefore, the exploration of catalytically active cluster species is of great significance to reveal detailed mechanisms and discover novel organic transformations.

In general, active metal cluster species are *in situ* generated during the induction period of metal-catalyzed reactions, which

Key Laboratory of Bioorganic Phosphorus Chemistry & Chemical Biology, Department of Chemistry, Tsinghua University, Beijing 100084, China. E-mail: zhaolchem@mail.tsinghua.edu.cn

are highly reactive and temporarily stabilized by reactants or additional ligands along with coordinative solvents as identified by mass spectroscopy.[5,18,19] However, metalated products formed in the late stage of catalytic reactions have been rarely explored regarding their particular role as catalytically active species. In this context, a vast number of Au(I)-catalyzed reactions bear much attention[20–22] because attractive aurophilic interaction between closed-shell d^{10} Au(I) atoms facilitates the formation of polyaurated reaction intermediates.[23–30] As gold(I) complexes act as a superior Lewis acid to activate unsaturated π-systems,[31] coordination of a substrate to Au(I) followed by the attack of a nucleophile often generates isolable organogold intermediates. They are generally believed to undergo a subsequent protodeauration process to output desired organic products and regenerate gold(I) catalytic species.[32–34] However, some isolated organogold intermediates featuring *gem*-diaurated motifs have been found resistant to the protodeauration-driven recycling process.[35–37] Therefore, structural evolution and catalytic activity investigations of metalated organic compounds based on stoichiometric gold-mediated organic transformations may provide new insights into the mechanism of Au(I) catalysis.

Herein, we report the isolation and structural characterization of a series of differently assembled organogold clusters based on Au(I)-mediated enyne cyclization reactions (Scheme 1). By using different σ-aurated enyne substrates, we obtain a discrete vicinal dicarbanion-bonded tetragold complex

Scheme 1 Assembly and catalytic behaviors of organometallic clusters.

$[Au_4(PPh_3)_4(L^{OMe})][NTf_2]_2$ (**2a**, L^{OMe} = 1,3-dimethoxyphenanthrene diide, and NTf_2 = bis-(trifluoromethanesulfonyl)imidate) and two assembled clusters $[Au_{11}(PPh_3)_6(L^{Ph})_4][NTf_2]_3$ (**2b**, L^{Ph} = 1-phenylnaphthalene diide) and $[Au_{28}(PPh_3)_8(L^{Me})_{12}]$ $[NTf_2]_4$ (**2c**, L^{Me} = 1-methylnaphthalene diide). Moreover, **2b** can undergo further transformation to form a tetradecanuclear cluster $[Au_{14}(PPh_3)_5(L^{Ph})_6][NTf_2]_2$ (**2d**). These discrete and assembled intermediates display four different pathways upon catalyzing the cyclization reaction of a 1,5-enyne substrate. **2a** undergoes a full protodeauration to generate unsaturated $[Au(PPh_3)]^+$ species for catalytic use. As for **2b**, a substrate-induced dissociation of the net-like Au_{11} core leads to a semi-stable Au_{10} unit and an active $[alkyne-Au(PPh_3)]^+$ fragment for further transformation (pathway I in Scheme 1). The Au_{10} cluster recombines with the recycling $[Au(PPh_3)]^+$ unit to recover the Au_{11} core. In contrast, **2c** initiates the catalytic reaction by exposing an unsaturated site through the cleavage of a Au–Au linkage in the dumbbell-like Au_{28} core (pathway II in Scheme 1). Lastly, the closed tetradecanuclear cluster **2d** with full ligand protection has no catalytic capacity.

Results and discussion

Synthesis and assembly of organogold(I) clusters

In view of the reported reaction pathway for enyne cyclization reactions,[38] we herein select σ-aurated alkyne compounds **1a**, **1b** and **1c** as substrates. As **1a** was treated with a stoichiometric amount of $[PPh_3Au](NTf_2)$ in 1,2-dichloroethane (DCE), the solution colour gradually changed from light yellow to yellow brown. Electrospray ionization mass spectroscopy (ESI-MS) of the reaction mixture revealed four peaks corresponding to polymetalated species $[Au_4(PPh_3)_4(L^{OMe})]^{2+}$, $[Au_3(PPh_3)_3(L^{OMe})]^+$, $[Au_3(PPh_3)_2(L^{OMe})]^+$, and $[Au_2(PPh_3)_2(L^{OMe}H)]^+$ (L^{OMe} = 1,3-dimethoxyphenanthrene diide) (Fig. S1†). Further screening suggested that the optimized 1 : 3 ratio of **1a** and $[PPh_3Au](NTf_2)$ gave a satisfactory isolated yield (35%) for the yellow crystalline compound **2a**. The formula of **2a** was determined as

$[(AuPPh_3)_4(L^{OMe})][NTf_2]_2$ by single-crystal X-ray diffraction analysis (Fig. 1a). **2a** has a phenanthrene dianionic center in a μ_4-C,C-η^2,η^2 mode to bind with a butterfly-shaped tetranuclear ring, which is further strengthened by a close Au–O interaction (2.7570(3) Å). The two carbanionic centers each attach to a *gem*-digold unit with the Au–C bond lengths in the range of 2.108(14)–2.214(12) Å, a bit longer than that of the reported CAu_2 species.[27,28,39–41] The Au–Au distances of the Au_4 unit can be classified into two shorter edges (2.7825(8) and 2.7859(8) Å) and two longer ones (2.9791(7) and 3.0472(8) Å). The crystal structure of **2a** is in good agreement with the detailed proton and phosphorus atom assignments as shown in the ^1H and ^{31}P NMR spectra (Fig. S4†). To understand the detailed electronic structure of **2a**, we performed adaptive natural density partitioning (AdNDP) analysis.[42] The AdNDP analysis explores that the $[C_2Au_4]$ unit of **2a** is composed of two σ-type 3c–2e and one pseudo-π-type 6c–2e bonds. These findings imply that the cluster formation is promoted by aurophilic interaction and multi-centered bonding between the 6s group orbitals of gold atoms and the 2p orbitals of carbon atoms (Fig. S6†).

Next, we investigated the transformation of **1b** as a representative alkenyl substrate. Under the same synthetic conditions as those for **1a**, the solution of **1b** turned brownish. The *in situ* ESI-MS analysis showed three distinct peaks, namely $[Au_2(PPh_3)_2(L^{Ph}H)]^+$, $[Au_3(PPh_3)_2(L^{Ph})]^+$, and $[Au_3(PPh_3)_3(L^{Ph})]^+$ (L^{Ph} = 1-phenylnaphthalene diide). However, no peaks corresponding to a similar tetranuclear cluster structure as observed in **2a** were detected (Fig. S7†). Diffusion of diethyl ether into the brown solution deposited orange crystals of **2b**, whose molecular formula was identified as $[Au_{11}(PPh_3)_6(L^{Ph})_4][NTf_2]_3$ by single-crystal X-ray diffraction analysis. As shown in Fig. 1b and S8,† **2b** shows a net-like Au_{11} structure that comprises four vicinal dicarbanion-bonded Au_4 quadrilaterals (I–VI) fused together by sharing five gold atoms. The remaining six unshared gold atoms are coordinated by a PPh_3 ligand each. Owing to steric hindrance, the four 1-phenylnaphthalene groups are alternatively located above (II and IV) and beneath (I and III) the extended Au_{11} plane. Therein, the Au–C bonds are in the range of 2.125(5)–2.193(6) Å (average 2.157 Å), comparable to the average bond length of **2a**. Notably, in comparison with the Au–Au distances of **2a**, **2b** has a shorter Au–Au edge in a CAu_2 moiety (average 2.714 Å), suggesting the formation of more robust *gem*-digold units. In addition, besides the low abundance peak of $[Au_{11}(PPh_3)_6(L^{Ph})_4]^{3+}$ in the ESI-MS spectrum of **2b**, a few prominent peaks were observed in the spectrum, indicating the presence of missing PPh_3 or $[Au(PPh_3)]^+$ species (Fig. S9†). This observation suggests that **2b** readily undergoes dissociation into smaller fragments under the conditions of mass spectroscopy. In contrast, the ^1H NMR spectrum of **2b** reveals a series of fine splitting peaks ranging from 5.8 to 8.9 ppm, and the ^{31}P NMR spectrum shows two peaks at 32.23 and 36.88 ppm corresponding to two inequivalent PPh_3 ligands as shown in the crystal structure of **2b** (Fig. S10†). This evidence demonstrates that the structure of **2b** in solution is consistent with its crystal structure.

Fig. 1 Synthesis, crystal structures and assembled patterns of (a) discrete vicinal dicarbanion-bonded tetragold cluster **2a**, (b) net-like cluster **2b**, and (c) dumbbell-like cluster **2c**. Hydrogen atoms, phenyl groups of PPh₃ ligands and peripheral NTf₂⁻ counter anions are omitted for clarity. Color coding: Au, orange and purple; C, gray; O, red; P, green.

To further understand the influence of ligands on cluster assembly, a new alkenyl substrate **1c** was introduced. In this case, the alkenyl α-position is substituted with a less bulky methyl group. This modification allows for a comparison of the ligand effect on the cluster assembly, providing insights into how different ligands impact the formation and structure of the clusters. The *in situ* ESI-MS analysis of the reaction mixture revealed several major peaks that can be assigned to bi- or tri-nuclear species such as $[Au_2(PPh_3)_2(L^{Me}H)]^+$ and $[Au_3(PPh_3)_3(L^{Me})]^+$ (Fig. S12†). Surprisingly, we also observed a minor peak

corresponding to a high-nuclear assembled species $[Au_{14}(PPh_3)_4(L^{Me})_6]^{2+}$. X-ray crystallographic analysis of the acquired complex **2c** revealed its molecular formula as $[Au_{28}(PPh_3)_8(L^{Me})_{12}][NTf_2]_4$. **2c** consists of two identical $[Au_{14}(PPh_3)_4(L^{Me})_6]^{2+}$ ($^{Me}Au_{14}$) fragments linked by a Au–Au linkage (3.0108(8) Å) and strengthened by two-fold π–π stacking between methylnaphthalenes ($D_{V-V'} = 3.965$ Å and $D_{VI-VI'} = 3.867$ Å, Fig. 1c and S13†). Theoretical studies show that these interactions provide a stabilization energy of 22.7 kcal mol⁻¹ (Fig. S14†). In view of the fact that the common Au–Au bond dissociation energy is

Fig. 2 (a) The **2b**-to-**2d** transformation and crystal structure of **2d**. Phenyl groups of PPh₃ ligands, hydrogen atoms, and peripheral NTf₂⁻ counter anions are omitted for clarity. Color coding: Au, yellow; C, gray; P, green. (b) (Left) The *in situ* ESI mass spectra of the crossover experiment between **2b** and **1b′**, and (right) ESI-MS of deposited microcrystals.

about 5–15 kcal mol⁻¹,[24] we conjecture that the π–π stacking of methylnaphthalene is an essential factor for stabilizing the dimeric form of **2c** (Fig. S15†).[43] Each closed-$^{Me}Au_{14}$ fragment is formed through the assembly of four vicinal dicarbanion-bonded Au₄ quadrilaterals (I, IV, V and VI) and two complementary Au₃ triangles (II and III) by sharing gold atoms. Additionally, two PPh₃-bonded gold atoms are attached to the fragment. This arrangement of shared gold atoms and bonding interactions contributes to the overall structure and stability of the $^{Me}Au_{14}$ fragment. In contrast to the assembled structure of **2b**, **2c** has slightly long Au–Au edges (average 2.730 and 3.084 Å for CAu₂ units and cross-unit edges, respectively) as well as long Au–C bonds (average 2.163 Å). The ESI-MS spectrum of **2c** displayed two dicationic cluster ion peaks at m/z = 2323.6321 and 2454.6816 that can be assigned to $[Au_{14}(PPh_3)_4(L^{Me})_6]^{2+}$ and $[Au_{14}(PPh_3)_5(L^{Me})_6]^{2+}$ ($^{Me}Au_{14}$-PPh₃), respectively (Fig. S16†). The obtained result indicates that the central Au–Au linkage in **2c** is susceptible to cleavage and thus yields two $^{Me}Au_{14}$ fragments.

Based on the discrete cluster structure in **2a** and assembled structures in **2b** and **2c**, we speculate that the driving force for assembly may originate from electronic properties of different *in situ* generated vicinal dicarbanions. It is expected that the moderate electron-donating ability of L^{Ph} and L^{Me} relative to L^{OMe} makes it insufficient to stabilize four positive $[AuPPh_3]^+$ units and causes further assembly of discrete aryl dianion-centered polygold units by sharing gold atoms. This assumption is also supported by the calculated atomic dipole moment corrected Hirshfeld population (ADCH) charges of two central

carbons in the basic $[C_2Au_4]$ units of **2a**, **2b** and **2c**. The sum of charges for **2a**, **2b** and **2c** is −0.556, −0.422 and −0.174, respectively, suggesting that the electronic nature of organic skeletons indeed has an important influence on the assembly of $[C_2Au_4]$ units. In addition, previous studies have illustrated that a *gem*-diaurated species decomposes into $[Au(PPh_3)_2]^+$ in the solution state.[35,44] Combined with *in situ* ESI-MS spectra, we propose that **1b** and **1c** first generate discrete $[C_2Au_3]$ units, and free $[Au(PPh_3)]^+$ seizes the PPh₃ ligand on $[C_2Au_3]$ to lead to $[Au(PPh_3)_2]^+$ and expose a Au site. The latter coordination unsaturation facilitates the occurrence of assembly.

In view of the open structure of **2b** relative to the closed architecture of **2c**, we speculate that the gold atoms in **2b** may also be accessible as a Lewis acid.[45–49] We then employed **2b** to activate the σ-aurated substrate **1b**. The ¹H NMR monitoring showed gradual disappearance of the alkenyl proton doublets of **1b** at 5.73 and 5.39 ppm (Fig. S21†). This process is accompanied by colour change from orange to deep red. Subsequently, diffusion of diethyl ether into the deep red solution led to red crystals of **2d** with the formula $[Au_{14}(PPh_3)_5(L^{Ph})_6][NTf_2]_2$ (Fig. 2a). The closed-Au₁₄ cluster core in **2d** is very similar to the $^{Me}Au_{14}$ of **2c**. Of note, all dianionic centers adopt a μ_3-C,C-η^1,η^2 mode to form several $[C_2Au_3]$ units. Thus, the structure of **2d** can be envisioned as six $[C_2Au_3]$ units fused together by sharing nine gold atoms. To complete the structure, vacant vertices of the fused cluster are filled with three equatorial and two axial $[AuPPh_3]^+$ units (Fig. S22†). In comparison with **2a–2c**, short Au–C distances (average 2.121 Å) in **2d** indicate strong interaction
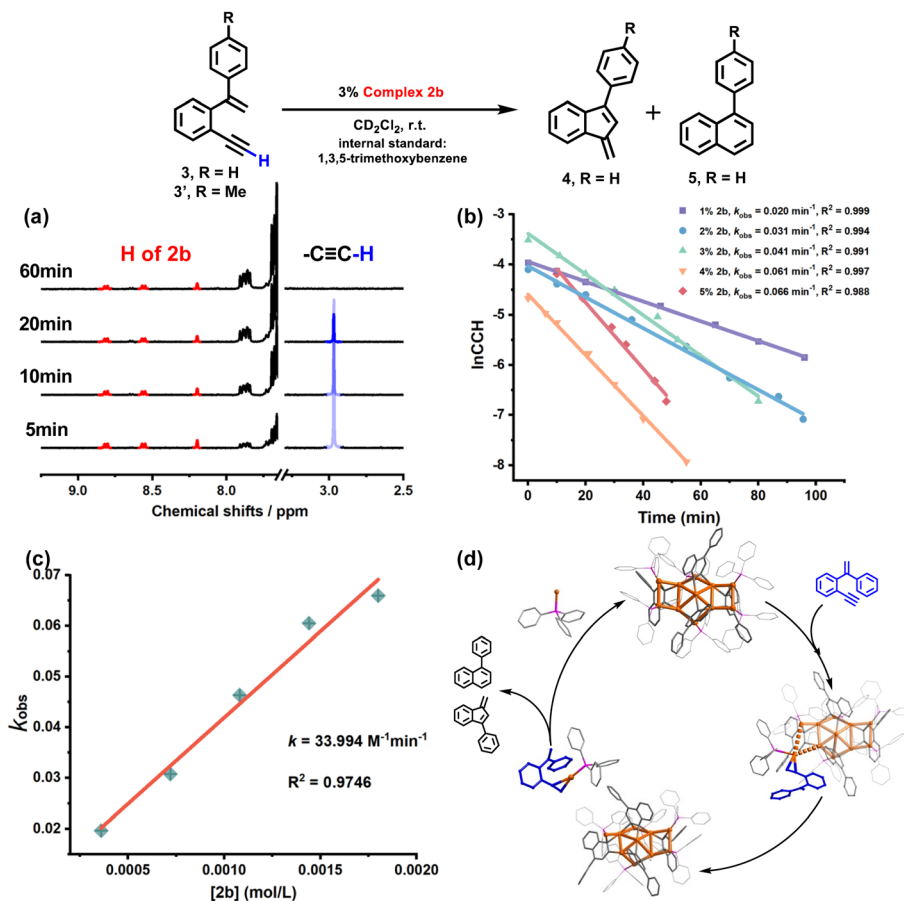
Fig. 3 (a) ^{1}H NMR monitoring of the **2b**-catalyzed cyclization reaction. Red and blue lines represent the proton NMR peaks of **2b** and the alkyne substrate, respectively. (b) Pseudo-first-order kinetic curves dependent on the concentration of **2b**. (c) Kinetic curves of **2b** dependent on the catalyst concentration. (d) Proposed mechanism for the cyclization reaction catalyzed by **2b**.

between organic skeletons and the central gold cluster core. Due to the existence of a tight layer of ligand protection, **2d** no longer has the ability to activate **1b** towards further structural transformation.

To further investigate the detailed construction process of **2d**, we performed a crossover experiment by using **2b** to activate the tolyl-substituted substrate **1b'**. The *in situ* ESI-MS spectrum discloses that **1b'** undergoes a similar cyclization to yield a tolyl-[C$_2$Au$_3$] species. Meanwhile, **2b** disrupts its assembled structure to regenerate many Ph-substituted [C$_2$Au$_3$] fragment species (Fig. 2b). Furthermore, diffusion of diethyl ether into the resulting maroon solution deposited crimson microcrystals. ESI-MS analysis on the microcrystal sample showed a normal distribution of Au$_{14}$ nanoclusters with a random combination of Ph- and tolyl-substituted [C$_2$Au$_3$] from 6 : 0 to 1 : 5 (Fig. 2b). We thus conceive that **2b** actually serves as a metastable species to dissociate and activate the transformation of substrates. Then, the newly formed Ph-substituted [C$_2$Au$_3$] units plus the dissociated species of **2b** promote the formation of the closed-cluster product **2d**.

Catalytic behaviors of organogold clusters

Inspired by the above **2b**-mediated cyclization of **1b** and **1b'**, we then tried to clarify the catalytic possibility of **2a–2d** in the cyclization reaction of 1,5-enynes. **2a–2d** show a typical butterfly-shaped, net-like, dumbbell-like and closed cluster structure, respectively. Upon the use of 3 mol% **2a** as catalyst, the cyclization of 1-ethynyl-2-(1-phenylvinyl)benzene (**3**) took place smoothly, which finally shows a high conversion ratio (>99%) and yields a mixture of two products **4** and **5** in a ratio of 4.5 : 1. Such selectivity is similar to the catalytic result (a 4 : 1 mixture) based on a mononuclear gold(ɪ) catalyst.[38] In the absence of **3**, **2a** kept its structure intact and stable as shown in the ^{1}H NMR monitoring (Fig. S24†). Nevertheless, the monitoring further showed that along with the catalytic reaction the characteristic peaks of **2a** gradually disappeared and the protodeaurated product 1,3-dimethoxyphenanthrene was simultaneously detected (Fig. S25†). Previous studies have revealed that the *gem*-diaurated species often experience the dissociation of a gold unit followed by protonolysis of the remaining Au–C bond to release organic products and recycle the mononuclear gold(ɪ) catalytic species.[36] We thus believe that **2a** undergoes a similar protodeauration process to generate [Au(PPh$_3$)]$^+$ units as a true catalytic species.

The **2b**-catalyzed cyclization of **3** also resulted in a mixture of **4** and **5** in a 4 : 1 ratio. However, in contrast to the full protodeauration process of **2a**, chemical shifts of **2b** in ^{1}H and [31]P

NMR spectra showed negligible change (Fig. 3a and S28†). After the reaction, **2b** could be recovered as a crystalline solid in a yield of 32%. Surprisingly, the catalyst loading can be lowered to 0.2 mol% such that the reaction proceeds with a turnover number (TON) of 403 (Fig. S29†). Subsequent kinetic studies based on ^{1}H NMR monitoring indicated that the decline of the alkyne proton signal at 2.97 ppm obeys pseudo-first-order kinetics. Along with the increase in catalyst loading from 1% to 5%, it also follows a first-order kinetic relationship dependent on the concentration of **2b** (Fig. 3b and c). Thus, the reaction orders of both substrate and catalyst are determined as one. We then employed ESI-MS to trace the entire reaction to make clear the true catalytic species. In order to avoid the interference of the organic skeleton of **2b** with the catalytic product of **3**, a tolyl-substituted substrate **3′** was used for a crossover experiment. The detection of a typical *gem*-diaurated species (*m/z* values of 1135.2021) as shown in many mononuclear gold-based catalysis demonstrates that [Au(PPh$_3$)]$^+$ may be the true catalytically active species (Fig. S30†). Accordingly, we conceive that a substrate molecule first attaches onto the Au$_{11}$ kernel and then induces its dissociation to generate a [alkyne-Au(PPh$_3$)]$^+$ fragment and a Au$_{10}$ unit. The former adduct further undergoes a 6-*endo*-dig or 5-*exo*-dig cyclization to give organic products. After the catalytic transformation, the Au$_{10}$ intermediate combines with the post reaction free [Au(PPh$_3$)]$^+$ unit by aurophilic interaction to rebuild the Au$_{11}$ compound **2b** (Fig. 3d and S31†).

As for the **2c**-catalyzed cyclization reaction (3 mol%), it displayed a very high conversion close to 100% and a 2 : 1 mixture of **4** and **5**. The unchanged chemical shifts and 17% crystal recovery of **2c** imply a catalytic process similar to that the **2b**-based one (Fig. S32†). And with 0.2 mol% loading of the catalyst, the TON of this reaction is 341 (Fig. S33†). However, ^{1}H NMR kinetic studies revealed that the **2c**-catalyzed reaction is a good fit with a pseudo-first-order of the substrate but a half-order with the catalyst concentration (Fig. S34†). As shown in the ESI-MS spectrum of **2c** (Fig. S16†), **2c** is prone to dissociating into two ^{Me}Au$_{14}$ and thereby exposes an unsaturated coordination site. During the catalytic reaction, the methyl proton signal of **2c** at 2.67 ppm changed from broad to narrow (Fig. S32†),
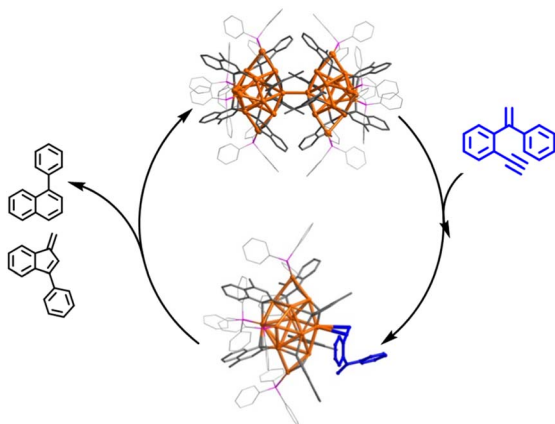

Fig. 4 Proposed mechanism for the activation of **3** by **2c**.

Table 1 The catalytic reaction results of **2a–2d**

Entry	Cluster	Conversion (%)	Selectivity (**4/5**)	TON
1	**2a**	>99	4.5 : 1	
2	**2b**	>99	4 : 1	403
3	**2c**	>99	2 : 1	341
4	**2d**	0	0	

which is probably ascribed to the conformational adjustment along with the cleavage of **2c** to ^{Me}Au$_{14}$. In addition, ESI-MS monitoring of the reaction mixture clearly shows characteristic signals of the dissociated species ^{Me}Au$_{14}$ (*m/z* 2323.6966) and ^{Me}Au$_{14}$-PPh$_3$ ([Au$_{14}$(PPh$_3$)$_5$(L^{Me})$_6$]$^{2+}$, *m/z* 2454.7042) and no peaks corresponding to any *gem*-diaurated species. The latter implies that no mononuclear gold species dissociate from **2c** (Fig. S35†). Consequently, we assume that the catalytic cycle of the dumbbell-like cluster **2c** is initiated by the cleavage of the central Au–Au linkage to produce two ^{Me}Au$_{14}$ units, each of which exposes a coordination unsaturated site to activate the alkyne group and complete the cyclization reaction (Fig. 4 and S36†).

In contrast, despite having a similar tetradecanuclear kernel as ^{Me}Au$_{14}$, the closed-cluster **2d** has no catalytic activity for **3** and other 1,5-enyne substrates (Fig. S37†). In view of the composition difference between ^{Me}Au$_{14}$ and **2d**, we believe that such catalytic inertness of **2d** should be ascribed to the loss of unsaturated Au site due to strong coordination of a PPh$_3$ ligand. Combining the above experiments, the catalytic performances of **2a–2d** are summarized in Table 1.

DFT calculations and mechanistic insight

To further rationalize our proposed mechanisms for the catalytic reactions of **2a–2c**, we then performed density functional theory (DFT) calculations to complement experimental kinetic studies. The geometry optimizations and single point energy calculations for the three catalytically active clusters and their intermediates in the respective key steps were conducted. First, we investigated the dissociation of a [Au(PPh$_3$)]$^+$ or PPh$_3$ moiety from **2a–2c**. In addition, the pathway for the dissociation of **2c** into two ^{Me}Au$_{14}$ units was considered as well (Fig. S38†). The calculated results suggest that the PPh$_3$ ligands strongly attach onto each metal cluster core with a very high dissociation energy (77.8–88.6 kcal mol^{-1}). Although the dissociation energy of a [Au(PPh$_3$)]$^+$ species out from the cluster cores of **2a–2c** is relatively small (29.6–47.6 kcal mol^{-1}), such a process is still energetically unfavored.

In accordance with the proposed mechanisms *vide supra*, we then designed new possible intermediates of the **2a** and **2b**-catalyzed reactions by dissociating a [alkyne-Au(PPh$_3$)]$^+$ species
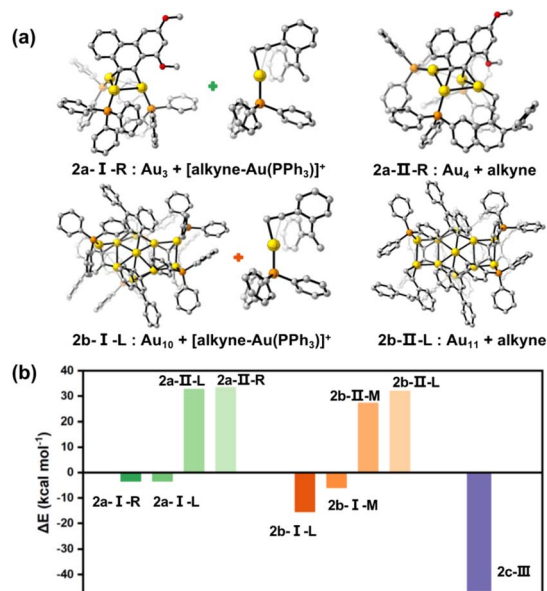
Fig. 5 DFT results for energies (kcal mol^{-1}) of intermediates of **2a–2c** according to the proposed mechanisms. (a) The calculated intermediate structures of **2a** and **2b** in the catalytic cyclization of enyne substrates. Only one dissociating site is shown here, and the other sites are shown in Fig. S39.† (b) Comparison of the energy differences for different activation types.

(type I in **2a-I** and **2b-I**) or replacing a PPh$_3$ on the cluster core by an alkyne substrate molecule (type II in **2a-II** and **2b-II**), respectively (Fig. 5a and S39†). Also, there are two chemically non-equivalent Au sites in each cluster structure that need to be considered. They are labelled as L(left)/R(right) in **2a** and L(left)/M(middle) in **2b**. As shown in Fig. 5b, the process to obtain the intermediate **2b-I** by forming a [alkyne-Au(PPh$_3$)]$^+$ species is exothermic, while the formation of the PPh$_3$-replaced intermediate **2b-II** needs a high energy of around 30 kcal mol^{-1}. Such a **2b-I**-based reaction pathway and cyclization reaction selectivity (Fig. S40 and S41†) are in agreement with the above experimental studies. Similar calculation studies on **2a** show the same trend in terms of energy requirements. Moreover, the formation of the favored **2a-I** possibly causes a subsequent protodeauration process to sequentially cleave the remaining carbon-polymetallic bonding and generate [AuPPh$_3$]$^+$ species for catalytic use. As for the **2c**-based transformation, the binding of an alkyne molecule with ^{Me}Au$_{14}$ largely compensates the energy requirement for the Au$_{28}$-to-^{Me}Au$_{14}$ dissociation in **2c** by breaking the central Au–Au linkage, finally reducing the single point energy change to −46.4 kcal mol^{-1} (Fig. 5b). Hence, these cluster intermediates with different architectures experience distinct bond breaking modes (Au–C and Au–Au for **2a** and **2b**; Au–Au for **2c**) in the same catalytic system, finally resulting in distinct catalytic pathways.

Conclusions

In summary, with the isolation of four vicinal dicarbanion-bonded organometallic clusters **2a–2d** from the cyclization of aurated enynes, we demonstrate that organogold clusters generated from the reaction transformation can be further assembled into nano-sized polynuclear clusters to function as catalytically active species. With the combination of detailed NMR kinetic monitoring, ESI-MS spectra, and DFT calculations, we illustrate that multiple aurophilic interactions and carbon–gold multi-center bonding in assemblies provide significant support for the stabilization of active intermediates. The differently assembled structures experience distinct pathways in the catalytic cyclization of enyne substrates. The dumbbell-like cluster **2c** tends to break the central Au–Au linkage to expose a catalytic site, while the net-like cluster **2b** drives the reaction by dissociating an [alkyne-Au(PPh$_3$)]$^+$ adduct from its Au$_{11}$ cluster core. The poor catalytic activity of the closed cluster **2d** may provide a rationale for catalyst deactivation in transition metal catalysis. Compared with the well-established synthesis of gold nanoclusters by reduction, this work presents a novel assembly pathway based on stoichiometric gold(ı)-mediated reactions. The assembly behavior observed in this context should also be taken into consideration when studying other systems with metallophilic interactions. Not only the field of gold catalysis, but other transition metal catalytic systems also require the scrutiny of such catalytically active organometal species.

Experimental

Materials and methods

2′-Iodoacetophenone, *o*-iodobenzophenone, 1-bromo-2-iodobenzene, 2-iodobenzoyl chloride and AgNTf$_2$ were purchased from Energy Chemical. Anhydrous tetrahydrofuran and Au(PPh$_3$)Cl were purchased from J&K Scientific. All other reagents and solvents were used without further purification. ^{1}H, ^{13}C and ^{31}P NMR were carried out on a JEOL ECX-400 MHz instrument. High resolution electrospray ionization mass spectrometry (ESI-MS) spectra were obtained on a Thermo Scientific Exactive Orbitrap instrument. The synthesis of σ-aurated substrates **1a–1c** and 1,5-enyne substrates **3–3′** is included in the ESI.†

Synthesis of complex 2a ([Au$_4$(PPh$_3$)$_4$(L^{OMe})][NTf$_2$]$_2$). A 1,2-dichloroethane solution (0.3 mL) of AgNTf$_2$ (11.64 mg, 0.03 mmol) was mixed with a 1,2-dichloroethane solution (0.3 mL) of PPh$_3$AuCl (14.85 mg, 0.03 mmol) and stirred at room temperature for 3 min. The supernatant was collected by centrifugation and was then added into a 1,2-dichloroethane (0.2 mL) solution of substrate **1a** (6.9 mg, 0.01 mmol). The mixture was further stirred for 8 hours and the solution color changed from light yellow to dark brown. After filtration, the filtrate was diffused using diethyl ether to obtain yellow crystals **2a** in 35% yield (9.2 mg). High-resolution ESI-MS: m/z = 1036.1708 for [Au$_4$(PPh$_3$)$_4$(L^{OMe})]$^{2+}$.

Synthesis of complex 2b ([Au$_{11}$(PPh$_3$)$_6$(L^{Ph})$_4$][NTf$_2$]$_3$). The synthetic procedure is similar to that of **2a** but with **1b** (6.6 mg, 0.01 mmol) instead of **1a**. After filtration and diffusion, orange crystals of **2b** were obtained in 21% yield (2.8 mg). High-resolution ESI-MS: m/z = 1515.8289 for [Au$_{11}$(PPh$_3$)$_6$(L^{Ph})$_4$]$^{3+}$.

Synthesis of complex 2c ([Au$_{28}$(PPh$_3$)$_8$(L^{Me})$_{12}$][NTf$_2$]$_4$). The synthetic procedure is similar to that of **2a** but with **1c** (6.0 mg,

0.01 mmol) instead of **1a**. After filtration and diffusion, crimson crystals of **2c** were obtained in 13% yield (1.1 mg). High-resolution ESI-MS: $m/z = 2323.6321$ for $[Au_{14}(PPh_3)_4(L^{Me})_6]^{2+}$.

Synthesis of complex 2d ([Au₁₄(PPh₃)₅(Lᴾʰ)₆][NTf₂]₂). In a 5 mL glass bottle, a mixture of substrate **1b** (6.6 mg, 0.01 mmol) and cluster **2b** (2.69 mg, 0.0005 mmol) was dissolved in anhydrous 1,2-dichloromethane (0.5 mL). The resulting mixture was stirred at room temperature for two days. After filtration, red crystals of **2d** were obtained by diffusing diethyl ether into the filtrate. Yield: 40% (1.0 mg) based on cluster **2b**. High-resolution ESI-MS: $m/z = 2640.2459$ for $[Au_{14}(PPh_3)_5(L^{Ph})_6]^{2+}$.

Computational details

Structures of all these clusters for calculation were built on the basis of single-crystal structures. Due to the huge system and the limitation of computing resources, the free energy calculation was replaced by single point energy. Geometry optimizations and single point energy calculations for all compounds were performed using the ORCA 5.0.2 program.[48,49] Geometry optimizations for the compounds considered here were optimized with the hybrid functional B3LYP[50,51] with Grimme GD3(BJ) dispersion correction[52,53] and the def2-SVP basis set.[54,55] Single point energy was calculated based on the optimized structures with the hybrid functional B3LYP with Grimme GD3(BJ) dispersion correction and a def2-SVP basis set for C, H, P and def2-TZVP basis set[54,55] for Au. To speed up the calculations, density fitting together with the chain of spheres approximations as implemented in ORCA (RIJCOSX)[56] was used, with the auxiliary basis def2/J.[57] The geometry of models was visualized using CYLview20 software.[58]

Molecular thermochemistry properties of mononuclear species were evaluated using the Gaussian 09 program.[59] Geometry optimizations as well as frequency calculations for all mononuclear species considered here were optimized with the hybrid functional B3LYP[50,51] with Grimme GD3(BJ) dispersion correction[52,53] and the def2-SVP basis set.[54,55] Geometric optimizations were performed without restriction in the experimental solvent dichloromethane. The integral equation formalism polarizable continuum (IEFPCM) solvation model with SMD radii[60] was used for solvent effect corrections. The optimized structures were confirmed to have no imaginary vibrational mode for intermediates and only one imaginary vibrational mode for each transition state. Transition states were further confirmed by connecting proper stationary points through intrinsic reaction coordinate (IRC) calculations. Thermal corrections were obtained by frequency calculations using the same method on optimized structures within the harmonic potential approximation under 298.15 K and 1 atm pressure. Single point energy was calculated based on the optimized structures with the hybrid functional B3LYP with Grimme GD3(BJ) dispersion correction and a def2-TZVP basis set.[54,55] AdNDP analysis[42] was performed using NBO 6.0 [61] and Multiwfn 3.8 software.[62] Hirshfeld,[63] Mulliken, and ADCH[64] atomic charges were calculated using Multiwfn 3.8 software. The molecular orbitals and AdNDP orbitals were visualized using Multiwfn 3.8 and VMD 1.9.3.[65]

Data availability

The X-ray crystallographic coordinates for structures reported in this article have been deposited at the Cambridge Crystallographic Data Centre (CCDC), under deposition numbers CCDC-2286449 (**2a**), CCDC-2286452 (**2b**), CCDC-2286453 (**2c**) and CCDC-2286454 (**2d**). For full characterization data including NMR and ESI-MS spectra and experimental details, see the ESI.† Any further relevant data are available from the authors upon reasonable request.

Author contributions

L. Z. conceived and supervised the project. The synthetic experiments, structural characterization, and catalytic studies were carried out by Q. L. DFT calculations were performed by X. Z. R. J. provided assistance in ESI-MS measurements. Q. L., X. Z., and L. Z. co-wrote the manuscript. All authors discussed the results.

Conflicts of interest

There are no conflicts to declare.

Acknowledgements

Notes and references

1 A. S. Kashin and V. P. Ananikov, *J. Org. Chem.*, 2013, **78**, 11117–11125.
2 D. B. Eremin and V. P. Ananikov, *Coord. Chem. Rev.*, 2017, **346**, 2–19.
3 L.-C. Liu and A. Corma, *Trends Chem.*, 2020, **2**, 383–400.
4 J. Oliver-Meseguer, J. R. Cabrero-Antonino, I. Domínguez, A. Leyva-Pérez and A. Corma, *Science*, 2012, **338**, 1452–1455.
5 A. Leyva-Perez, J. Oliver-Meseguer, P. Rubio-Marques and A. Corma, *Angew. Chem., Int. Ed.*, 2013, **52**, 11554–11559.
6 J. Oliver-Meseguer, A. Leyva-Pérez and A. Corma, *ChemCatChem*, 2013, **5**, 3509–3515.
7 J. Oliver-Meseguer, L. Liu, S. Garcia-Garcia, C. Canos-Gimenez, I. Dominguez, R. Gavara, A. Domenech-Carbo, P. Concepcion, A. Leyva-Perez and A. Corma, *J. Am. Chem. Soc.*, 2015, **137**, 3894–3900.
8 M. Neumeier, U. Chakraborty, D. Schaarschmidt, V. de la Pena O'Shea, R. Perez-Ruiz and A. Jacobi von Wangelin, *Angew. Chem., Int. Ed.*, 2020, **59**, 13473–13478.
9 C.-H. Li, S. Song, Y.-L. Li, C. Xu, Q.-Q. Luo, Y.-L. Guo and X.-M. Wang, *Nat. Commun.*, 2021, **12**, 3813.
10 E. Bayram, J. C. Linehan, J. L. Fulton, J. A. Roberts, N. K. Szymczak, T. D. Smurthwaite, S. Ozkar, M. Balasubramanian and R. G. Finke, *J. Am. Chem. Soc.*, 2011, **133**, 18889–18902.
11 J. Cordon, G. Jimenez-Oses, J. M. Lopez-de-Luzuriaga and M. Monge, *Nat. Commun.*, 2017, **8**, 1657.

12 T. N. Gieshoff, U. Chakraborty, M. Villa and A. Jacobi von Wangelin, *Angew. Chem., Int. Ed.*, 2017, **56**, 3585–3589.

13 Y. S. Panova, A. S. Kashin, M. G. Vorobev, E. S. Degtyareva and V. P. Ananikov, *ACS Catal.*, 2016, **6**, 3637–3643.

14 B. D. Briggs, N. M. Bedford, S. Seifert, H. Koerner, H. Ramezani-Dakhel, H. Heinz, R. R. Naik, A. I. Frenkel and M. R. Knecht, *Chem. Sci.*, 2015, **6**, 6413–6419.

15 D. Canseco-Gonzalez, A. Gniewek, M. Szulmanowicz, H. Muller-Bunz, A. M. Trzeciak and M. Albrecht, *Chem.–Eur. J.*, 2012, **18**, 6055–6062.

16 S. Sandl, F. Schwarzhuber, S. Pollath, J. Zweck and A. Jacobi von Wangelin, *Chem.–Eur. J.*, 2018, **24**, 3403–3407.

17 M. A. Rivero-Crespo, A. Leyva-Perez and A. Corma, *Chem.–Eur. J.*, 2017, **23**, 1702–1708.

18 X.-F. Jiang, H. Huang, Y.-F. Chai, T. L. Lohr, S.-Y. Yu, W. Lai, Y.-J. Pan, M. Delferro and T. J. Marks, *Nat. Chem.*, 2016, **9**, 188–193.

19 B. L. Tran, J. L. Fulton, J. C. Linehan, J. A. Lercher and R. M. Bullock, *ACS Catal.*, 2018, **8**, 8441–8449.

20 A. S. K. Hashmi, *Chem. Rev.*, 2007, **107**, 3180–3211.

21 R. Dorel and A. M. Echavarren, *Chem. Rev.*, 2015, **115**, 9028–9072.

22 L. Fensterbank and M. Malacria, *Acc. Chem. Res.*, 2014, **47**, 953–965.

23 H. Schmidbaur and A. Schier, *Chem. Soc. Rev.*, 2008, **37**, 1931–1951.

24 (*a*) H. Schmidbaur and A. Schier, *Chem. Soc. Rev.*, 2012, **41**, 370–412; (*b*) N. Mirzadeh, S. H. Priver, A. J. Blake, H. Schmidbaur and S. K. Bhargava, *Chem. Rev.*, 2020, **120**, 7551–7591.

25 Z.-N. Wu, Y.-H. Du, J.-L. Liu, Q.-F. Yao, T.-K. Chen, Y.-T. Cao, H. Zhang and J.-P. Xie, *Angew. Chem., Int. Ed.*, 2019, **58**, 8139–8144.

26 Q.-S. Zheng, S. Borsley, G. S. Nichol, F. Duarte and S. L. Cockroft, *Angew. Chem., Int. Ed.*, 2019, **58**, 12617–12623.

27 T. A. Nguyen, E. Daiann Sosa Carrizo, H. Cattey, P. Fleurat-Lessard, J. Roger and J. C. Hierso, *Chem.–Eur. J.*, 2022, **28**, e202200769.

28 E. S. Smirnova and A. M. Echavarren, *Angew. Chem., Int. Ed.*, 2013, **52**, 9023–9026.

29 J. Yuan, T.-T. Sun, X. He, K. An, J. Zhu and L. Zhao, *Nat. Commun.*, 2016, **7**, 11489.

30 K. Xiao, Y. Xue, B. Yang and L. Zhao, *CCS Chem.*, 2021, **3**, 555–565.

31 D. J. Gorin and F. D. Toste, *Nature*, 2007, **446**, 395–403.

32 E. Soriano and J. Marco-Contelles, *Acc. Chem. Res.*, 2009, **42**, 1026–1036.

33 E. Jiménez-Núñez and A. M. Echavarren, *Chem. Rev.*, 2008, **108**, 3326–3350.

34 A. Collado, D. J. Nelson and S. P. Nolan, *Chem. Rev.*, 2021, **121**, 8559–8612.

35 G. Seidel, C. W. Lehmann and A. Furstner, *Angew. Chem., Int. Ed.*, 2010, **49**, 8466–8470.

36 A. S. Hashmi, I. Braun, P. Nosel, J. Schadlich, M. Wieteck, M. Rudolph and F. Rominger, *Angew. Chem., Int. Ed.*, 2012, **51**, 4456–4460.

37 D. Weber, M. A. Tarselli and M. R. Gagne, *Angew. Chem., Int. Ed.*, 2009, **48**, 5733–5736.

38 T. Shibata, Y. Ueno and K. Kanda, *Synlett*, 2006, **2006**, 0411–0414.

39 K. Xiao, Y. Zhao, J. Zhu and L. Zhao, *Nat. Commun.*, 2019, **10**, 5639.

40 Q.-H. Wei, L.-Y. Zhang, G.-Q. Yin, L.-X. Shi and Z.-N. Chen, *J. Am. Chem. Soc.*, 2004, **126**, 9940–9941.

41 W.-D. Si, C.-K. Zhang, M. Zhou, Z. Wang, L. Feng, C.-H. Tung and D. Sun, *Sci. Adv.*, 2024, **10**, eadm6928.

42 D. Y. Zubarev and A. I. Boldyrev, *Phys. Chem. Chem. Phys.*, 2008, **10**, 5207–5217.

43 Q.-F. Yao, L.-M. Liu, S. Malola, M. Ge, H.-Y. Xu, Z.-N. Wu, T.-K. Chen, Y. T. Cao, M. F. Matus, A. Pihlajamäki, Y. Han, H. Häkkinen and J.-P. Xie, *Nat. Chem.*, 2023, **15**, 230–239.

44 J. E. Heckler, M. Zeller, A. D. Hunter and T. G. Gray, *Angew. Chem., Int. Ed.*, 2012, **51**, 5924–5928.

45 G. Li, H. Abroshan, Y.-X. Chen, R.-C. Jin and H. J. Kim, *J. Am. Chem. Soc.*, 2015, **137**, 14295–14303.

46 R. R. Nasaruddin, Q.-F. Yao, T.-K. Chen, M. J. Hülsey, N. Yan and J.-P. Xie, *Nanoscale*, 2018, **10**, 23113–23121.

47 J.-H. Yu, Z.-R. Yuan, J. Xu, J.-G. Wang, T.-D. Li, Y.-Z. Li and D. Sun, *Chem. Sci.*, 2023, **14**, 6564–6571.

48 F. Neese, *Wiley Interdiscip. Rev.: Comput. Mol. Sci.*, 2022, **12**, e1606.

49 F. Neese, F. Wennmohs, U. Becker and C. Riplinger, *J. Chem. Phys.*, 2020, **152**, 224108.

50 A. D. Becke, *J. Chem. Phys.*, 1993, **98**, 5648–5652.

51 C. Lee, W. Yang and R. G. Parr, *Phys. Rev. B: Condens. Matter Mater. Phys.*, 1988, **37**, 785–789.

52 S. Grimme, S. Ehrlich and L. Goerigk, *J. Comput. Chem.*, 2011, **32**, 1456–1465.

53 S. Grimme, J. Antony, S. Ehrlich and H. Krieg, *J. Chem. Phys.*, 2010, **132**, 154104.

54 F. Weigend and R. Ahlrichs, *Phys. Chem. Chem. Phys.*, 2005, **7**, 3297–3305.

55 D. Andrae, U. Häußermann, M. Dolg, H. Stoll and H. Preuß, *Theor. Chim. Acta*, 1990, **77**, 123–141.

56 F. Neese, F. Wennmohs, A. Hansen and U. Becker, *Chem. Phys.*, 2009, **356**, 98–109.

57 F. Weigend, *Phys. Chem. Chem. Phys.*, 2006, **8**, 1057–1065.

58 C. Y. Legault, *CYLview20*, Université de Sherbrooke, 2020, https://www.cylview.org.

59 M. J. Frisch, G. W. Trucks, H. B. Schlegel, G. E. Scuseria, M. A. Robb, J. R. Cheeseman, G. Scalmani, V. Barone, B. Mennucci, G. A. Petersson, H. Nakatsuji, M. Caricato, X. Li, H. P. Hratchian, A. F. Izmaylov, J. Bloino, G. Zheng, J. L. Sonnenberg, M. Hada, M. Ehara, K. Toyota, R. Fukuda, J. Hasegawa, M. Ishida, T. Nakajima, Y. Honda, O. Kitao, H. Nakai, T. Vreven, J. A. Montgomery Jr, J. E. Peralta, F. Ogliaro, M. Bearpark, J. J. Heyd, E. Brothers, K. N. Kudin, V. N. Staroverov, R. Kobayashi, J. Normand, K. Raghavachari, A. Rendell, J. C. Burant, S. S. Iyengar, J. Tomasi, M. Cossi, N. Rega, J. M. Millam, M. Klene, J. E. Knox, J. B. Cross, V. Bakken, C. Adamo, J. Jaramillo, R. Gomperts, R. E. Stratmann, O. Yazyev, A. J. Austin, R. Cammi, C. Pomelli, J. W. Ochterski,

R. L. Martin, K. Morokuma, V. G. Zakrzewski, G. A. Voth, P. Salvador, J. J. Dannenberg, S. Dapprich, A. D. Daniels, Ö. Farkas, J. B. Foresman, J. V. Ortiz, J. Cioslowski and D. J. Fox, *Gaussian 09, revision E.01*, Gaussian, Inc., Wallingford, CT, 2013.

60 A. V. Marenich, C. J. Cramer and D. G. Truhlar, *J. Phys. Chem. B*, 2009, **113**, 6378–6396.

61 E. D. Glendening, C. R. Landis and F. Weinhold, *J. Comput. Chem.*, 2013, **34**, 1429–1437.

62 T. Lu and F. Chen, *J. Comput. Chem.*, 2012, **33**, 580–592.

63 F. L. Hirshfeld, *Theor. Chim. Acta*, 1977, **44**, 129–138.

64 T. Lu and F. Chen, *J. Theor. Comput. Chem.*, 2012, **11**, 163–183.

65 W. Humphrey, A. Dalke and K. Schulten, *J. Mol. Graphics*, 1996, **14**, 33–38.